New Polarimetric Radar Algorithm for Melting-Layer Detection and Determination of Its Height

ALEXANDER RYZHKOV[a,b] AND JOHN KRAUSE[a,b]

[a] *Cooperative Institute for Mesoscale Meteorological Studies, University of Oklahoma, Norman, Oklahoma*
[b] *NOAA/National Severe Storms Laboratory, Norman, Oklahoma*

(Manuscript received 15 September 2021, in final form 21 December 2021)

ABSTRACT: A novel polarimetric radar algorithm for melting-layer (ML) detection and determination of its height has been developed and tested for a large number of cold-season weather events. The algorithm uses radial profiles of the cross-correlation coefficient (ρ_{hv} or CC) at the lowest elevation angles (<5°–6°). The effects of beam broadening on the spatial distribution of CC have been taken into account via theoretical simulations of the radial profiles of CC assuming intrinsic vertical profiles of polarimetric radar variables within the ML with varying heights and depths of the ML. The model radial profiles of CC and their key parameters are stored in lookup tables and compared with the measured CC profiles. The matching of the model and measured CC radial profiles allows the algorithm to determine the "true" heights of the top and bottom of the ML, H_t and H_b, at distances up to 150 km from the radar. Integrating the CC information from all available antenna elevations makes it possible to produce accurate maps of H_t and H_b over large areas of radar coverage as opposed to the previous ML detection methods including the existing algorithm implemented on the U.S. network of the WSR-88Ds. The initial version of the algorithm has been implemented in C++ and tested for a multitude of cold-season weather events characterized by a low ML with different degrees of spatial nonuniformity including cases with sharp frontal boundaries and rain–snow transitions. The new ML detection algorithm (MLDA) exhibits robust performance, demonstrating spatial and temporal continuity, and showing general consistency of the ML designations matching those obtained from the regional model and the quasi-vertical profiles (QVP) methodology output.

KEYWORDS: Radars/Radar observations; Remote sensing; Weather radar signal processing

1. Introduction

The quality of hydrometeor classification and quantitative precipitation estimation performed by modern operational polarimetric weather radars is contingent on an accurate melting-layer (ML) designation. Polarimetric characteristics of dry snow above the ML are quite similar to the ones of light to moderate rain below the ML; therefore, it is important to determine the location of the ML in order to distinguish between snow in the cold part of the cloud and rain in its warmer part, a designation needed for reliable hydrometeor identification. Dangerous cold-season events such as freezing rain/drizzle are often associated with an elevated temperature inversion or "warm tongue," where the warm air is on top of a subfreezing surface layer. Snow falling from the upper part of the cloud may completely or partially melt (e.g., Reeves et al. 2016), while traversing this warmer layer. The absence of the ML signifies either pure ice or pure snow in a full vertical column of the atmosphere or shallow warm rain or drizzle when precipitation is formed at the positive temperatures. Absence of an ML may also signify a lack of data collected because of storm location or gaps in the radar's scanning strategy.

Knowing the height and depth of the ML is important for quantitative precipitation estimation (QPE) because mixed-phase and frozen hydrometeors sampled by the radar may contaminate rainfall estimates. Popular QPE techniques based on specific attenuation A and specific differential phase K_{DP} are not valid in areas affected by the "brightband" contamination or beam overshooting when the radar resolution volume is within the ML or above it. Knowledge of the ML location is also important for the microphysical characterization of the cloud, including the separation of liquid from frozen hydrometeors and the evaluation of icing potential. Satellite techniques for precipitation measurements have to account for the impact of the ML and are critically dependent on the accuracy of the ML designation.

The melting layer is characterized by very pronounced polarimetric radar signatures such as notable enhancements of the radar reflectivity Z, differential reflectivity Z_{DR}, and linear depolarization ratio LDR and a reduction of the cross-correlation coefficient ρ_{hv} (or CC—the abbreviation used throughout this article) (Ryzhkov and Zrnić 2019). This is why the polarimetric weather radars are very efficient for identification and quantification of the ML. Various techniques for polarimetric ML detection with polarimetric scanning radars have been suggested in a number of studies (Brandes and Ikeda 2004; Tabary et al. 2006; Matrosov et al. 2007, 2017; Giangrande et al. 2008; Boodoo et al. 2010; Schuur et al. 2012; Wolfensberger et al. 2016; Allabakash et al. 2019; Shusse et al. 2019). Vertically pointing cloud radars capable of measuring LDR are also utilized for accurate estimation of the ML height above the radar (e.g., Song et al. 2021).

One of the first polarimetric techniques for ML detection was proposed by Brandes and Ikeda (2004) for utilization at S band. Their methodology is based on the matching of the observed vertical profiles of Z, LDR, and CC through the ML

Corresponding author: Alexander Ryzhkov, alexander.ryzhkov@noaa.gov

DOI: 10.1175/JTECH-D-21-0130.1

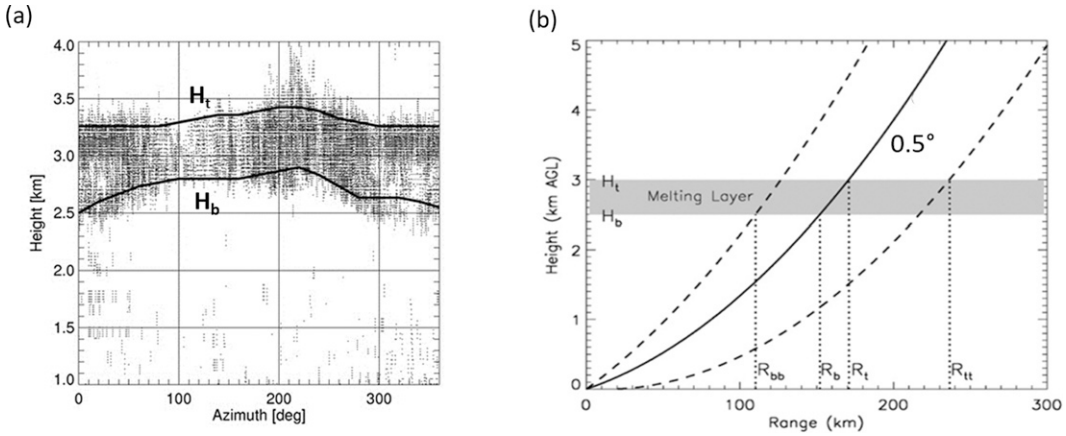

FIG. 1. (a) The ML points mapped on the height–azimuth plane. The 80% (ML top, H_t) and 20% (ML bottom, H_b) height contours are overlaid in solid lines. (b) Geometry of the radar beam with respect to the melting layer. The beam axis is drawn with the thick solid curve, whereas the locations of the ±0.5° beam extent are indicated with the dashed curves.

with their idealized model profiles. A similar technique using a sole vertical profile of CC was used by Tabary et al. (2006) for operational ML identification at C band. Matrosov et al. (2007, 2017) also utilized the cross-correlation coefficient for detecting ML at X and S bands. Wolfensberger et al. (2016) recommended to use the product of Z (expressed in a linear scale) and the difference (1 − CC) for ML designation at X band.

The melting-layer detection algorithm (MLDA) currently implemented on the operational WSR-88D network in the United States is based on the methodology proposed by Giangrande et al. (2008) that prescribes analysis of the radial profiles of Z, Z_{DR}, and CC at antenna elevations between 4° and 10°. A similar technique was later adapted for C-band radar data in Canada (Boodoo et al. 2010). The problem with all existing methodologies for ML detection is that only the radar data collected in a close proximity to the radar are utilized and, as a result, designation of the ML is made at relatively close distances from the radar. For example, Matrosov et al. (2017) utilize the data from antenna tilt at 5.1°, which allows reliable estimation of the ML height at ranges up to 13–15 km from the radar. Wolfensberger et al. (2016) and Allabakash et al. (2019) used the radar data with fine vertical resolution collected in the range–height indicator (RHI) mode of operation and were able to derive good-quality information about the ML with maximal range of about 20 km. Modern operational weather radars usually do not practice "genuine" RHIs and the quality of RHIs reconstructed from the plan position indicator (PPI) scans at various elevation angles is not sufficient for reliable ML quantification.

To detect and quantify an ML at longer distances (beyond 20 km), the data from lower antenna tilts (down to 0.5°) have to be used. However, this requires taking into account the effects of antenna beam broadening on the ML polarimetric signatures, which has never been done before. This is the primary reason that existing algorithms are not able to produce *2D maps* of the ML height over sufficiently large radar coverage areas, say, up to 150–200 km from the radar. This challenge motivates the current study in which we propose a new polarimetric radar algorithm for melting-layer detection and determination of its height that utilizes the data from lowest antenna elevations, accounts for beam broadening effects at longer distances from the radar, and generates the 2D horizontal maps of the heights of the bottom and the top of the melting layer up to 150 km from the radar.

The paper is organized as follows. In section 2, the deficiencies of the current operational MLDA are discussed and the description of the novel MLDA algorithm is provided. Section 3 contains examples of the practical implementation of the new MLDA followed by section 4 with results of validation. A discussion and conclusions are presented in section 5.

2. New algorithm description

a. Deficiencies of the existing WSR-88D MLDA

According to the existing MLDA currently implemented on the WSR-88D network, the radial profiles of Z, Z_{DR}, and CC are examined at each azimuth and at all elevations between 4° and 10°. For every radial, the range gates belonging to the ML are identified following the rules described in Giangrande et al. (2008). For each ML range gate, its height is determined as presented in a height versus azimuth plane in Fig. 1a. At every azimuth, the heights of the ML bottom and top H_b and H_t are determined as the altitudes corresponding to the 20th and 80th percentiles of the distribution of the ML points' heights. The resulting solid curves in Fig. 1a represent the azimuthal dependencies of H_b and H_t. In other words, the algorithm captures the azimuthal dependence of the ML height if it occurs in a relatively small area surrounding the radar. For a typical range of ML heights during the cold season from 1 to 2 km, the corresponding radius of the representative area is between 14 and 28 km. This means that any azimuthal and radial nonuniformity of the ML beyond these distances, such as an approaching cold front, is not captured

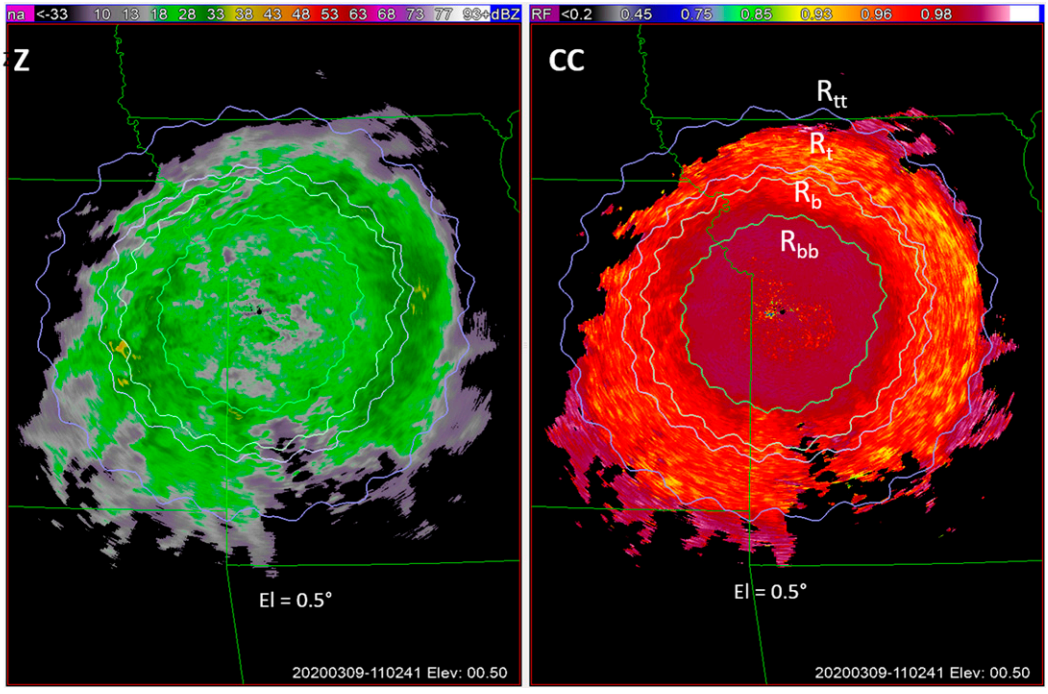

FIG. 2. PPIs of (left) Z and (right) CC at El = 0.5° for the storm on 9 Mar 2020 observed by the KEAX WSR-88D at 1102 UTC with the contours of R_{tt}, R_t, R_b, and R_{bb} overlaid.

by the existing algorithm. Nevertheless, the values of H_b and H_t obtained over this relatively small area are used to predict the ranges at which the upper and lower parts of the radar beam intercept the ML at the lowest tilt of 0.5° assuming radial homogeneity of the ML over the whole radar field of view (Fig. 1b). The azimuthal dependencies of these ranges (R_{bb}, R_b, R_t, and R_{tt}) are usually overlaid on the PPI fields of different radar variables (e.g., Z and CC in Fig. 2). The results of the hydrometeor classification by the fuzzy logic algorithm on the WSR-88D network are then checked for consistency with range location of the ML (Park et al. 2009). For example, no snow is allowed for $R < R_{bb}$ and no rain is permitted for $R > R_b$. There is little doubt that the results of such echo classification might be erroneous if significant changes in the height of the ML occur farther away from the radar.

An example of hydrometeor misclassification due to inadequate determination of the ML height is illustrated in Fig. 3. Three top panels in Fig. 3 represent PPIs of Z, Z_{DR}, and CC at El = 4.0° for the storm on 5 February 2020 in Oklahoma observed by the KTLX WSR-88D at 1105 UTC. There is no ML signature visible at El = 4.0°. Some enhancement of Z_{DR} and reduction in CC at the periphery of the echo are not related to the ML. These are associated with the dendritic growth layer (DGL) usually located within the temperature interval between −10° and −20°C. Using the information at the 4° and higher tilts, the existing MLDA algorithm would classify snow everywhere in the radar coverage area. However, the PPIs of the same variables at El = 1.3° (bottom panels in Fig. 3) clearly indicate the presence of the frontal boundary in terms of Z_{DR} and CC southeast of the radar, which clearly separates pure snow at the surface in the NW sector and wet snow and rain in the SE sector.

b. *Description of a new MLDA*

The main idea of a new MLDA method is to use the CC data from *all* antenna tilts below 5°–6° and compare the measured radial profiles of CC with the simulated (modeled) ones computed for various heights and depths of the ML. Matching the measured radial profiles of CC with the simulated ones allows finding the intrinsic (true) parameters of the ML in the range interval corresponding to a CC dip at a given antenna elevation. In fact, instead of matching full radial profiles of CC, their key parameters such as the distance to the beginning of the CC dip and the "strength" of the dip are used in the matching routine. The simulated radial profiles of CC and their parameters are stored in the precalculated lookup tables, which have to be *generated only once*. Next we explain how the radial CC profiles are simulated and how the lookup tables are generated.

A radial profile of CC depends on the intrinsic ("true") vertical profiles of polarimetric radar variables within the ML. In this paper, we distinguish between intrinsic values of the cross-correlation coefficient (ρ_{hv}), simulated measured values [$\rho_{hv}^{(m)}$], and actually observed values (CC). In our simulations, intrinsic vertical profiles of Z and ρ_{hv} and other pertinent polarimetric variables are modeled as piecewise linear functions parameterized by a number of microphysical parameters (Fig. 4). The impact of beam broadening on the vertical and radial profiles of Z and $\rho_{hv}^{(m)}$ is quantified using the formulas

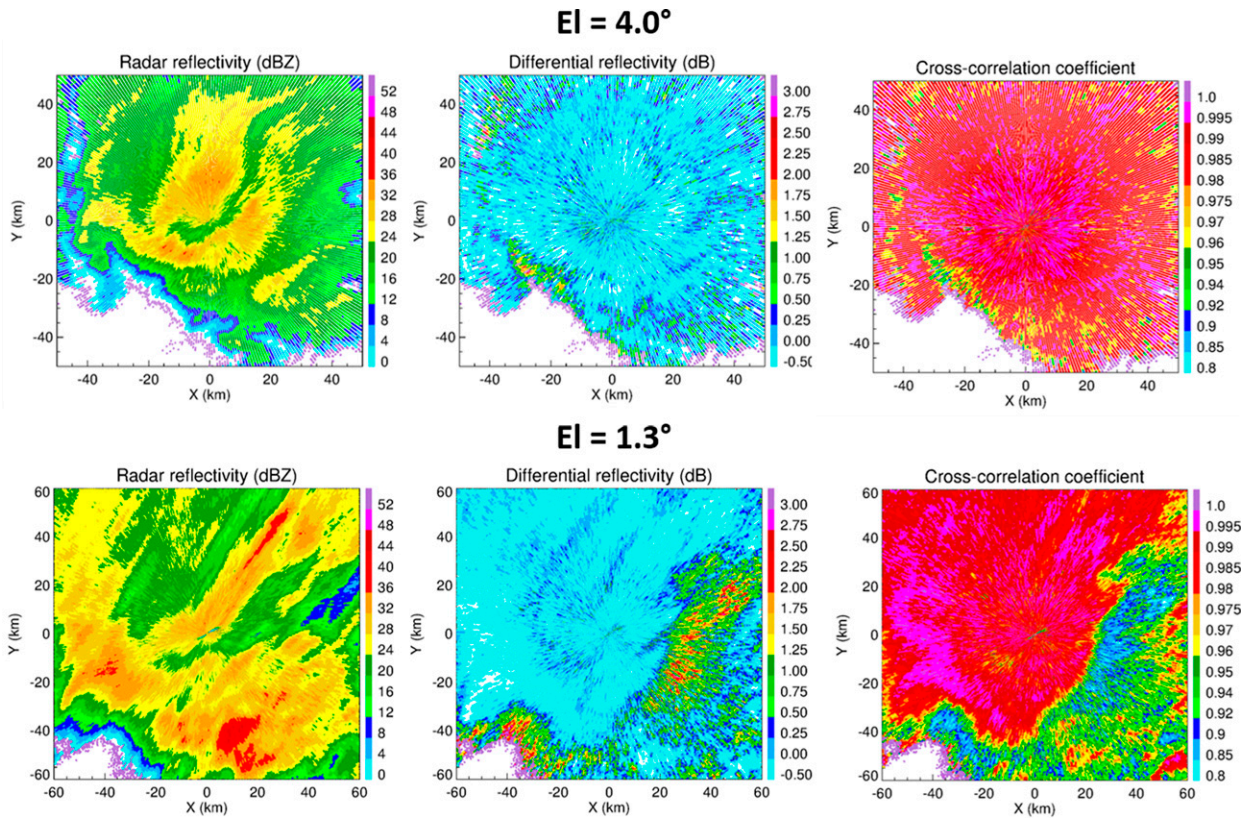

FIG. 3. PPIs of Z, Z_{DR}, and CC at (top) El = 4.0° and (bottom) El = 1.3° for the storm on 5 Feb 2020 in Oklahoma observed by the KTLX WSR-88D at 1105 UTC.

from Ryzhkov (2007). The measured radar reflectivity factors $Z^{(m)}_{h,v}(\mathbf{r}_0)$ at horizontal and vertical polarizations at location $\mathbf{r}_0$ is

$$Z^{(m)}_{h,v}(\mathbf{r}_0) = \int Z_{h,v}(\mathbf{r}) I(\mathbf{r}, \mathbf{r}_0) d\mathbf{r}, \tag{1}$$

where $Z_{h,v}$ are intrinsic (true) values of radar reflectivity at orthogonal polarizations and $I(\mathbf{r}, \mathbf{r}_0)$ is an "illumination function" depending on the size and shape of the radar sampling volume centered at $\mathbf{r}_0$. The function $I(\mathbf{r}, \mathbf{r}_0)$ is determined by the radar pulse length and the width of the radar beam at $\mathbf{r}_0$ (Ryzhkov 2007, appendix). The measured cross-correlation coefficient at location $\mathbf{r}_0$ is given by the ratio

$$\rho^{(m)}_{hv}(\mathbf{r}_0) = \frac{\left|R^{(m)}_{hv}(\mathbf{r}_0)\right|}{\left[Z^{(m)}_{h}(\mathbf{r}_0) Z^{(m)}_{v}(\mathbf{r}_0)\right]^{1/2}}, \tag{2}$$

where $R^{(m)}_{hv}(\mathbf{r}_0)$ is the measured complex covariance

$$R^{(m)}_{hv}(\mathbf{r}_0) = \int R_{hv}(\mathbf{r}) I(\mathbf{r}, \mathbf{r}_0) d\mathbf{r}. \tag{3}$$

The intrinsic complex covariance depends on several radar variables (Ryzhkov et al. 2017):

$$R_{hv} = Z_h Z_{dr}^{-1/2} \rho_{hv} \exp\left\{j\left[\Phi_{DP} - \Phi^{(t)}_{DP} - \Phi^{(r)}_{DP}\right]\right\} + Z_h L_{dr} \exp\left\{j\left[\Phi^{(t)}_{DP} - \Phi^{(r)}_{DP}\right]\right\}, \tag{4}$$

where Z_{dr} is the differential reflectivity expressed in linear scale, L_{dr} is the linear depolarization ratio in linear scale, Φ_{DP} is the differential phase on propagation, $\Phi^{(t)}_{DP}$ is the system differential phase on transmission, and $\Phi^{(r)}_{DP}$ is the system differential phase on reception. If the effects of cross coupling can

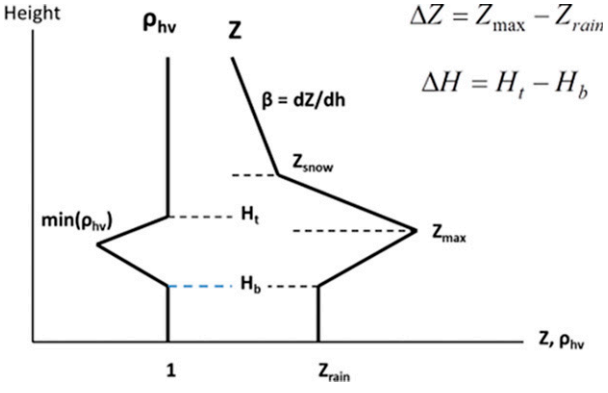

FIG. 4. A model of intrinsic vertical profiles of ρ_{hv} and Z within the melting layer used for simulations.

be neglected (i.e., L_{dr} is small), the second term in (4) can be ignored and the absolute value of $\rho_{hv}^{(m)}(\mathbf{r}_0)$ depends on Z_h, Z_{dr}, and ρ_{hv} only. It is important that the impact of beam broadening on $\rho_{hv}^{(m)}$ cannot be quantified by the computation of the integral $\rho_{hv}^{(m)}(\mathbf{r}_0) = \int \rho_{hv}(\mathbf{r}) I(\mathbf{r}, \mathbf{r}_0) d\mathbf{r}$ similar to the radar reflectivity in Eq. (1). Instead, the value of $\rho_{hv}^{(m)}(\mathbf{r}_0)$ depends on the product $Z_h Z_{dr}^{-1/2} \rho_{hv}$ and the vertical profile of Z_{dr} should be also modeled.

We compute $Z_{h,v}^{(m)}$ and $\rho_{hv}^{(m)}$ using Eqs. (1)–(4) at arbitrary antenna elevation for 25 heights of the bottom of the ML (H_b) and 8 values of minimal ρ_{hv} in the ML $\left[\rho_{hv}^{(min)}\right]$—see Fig. 4. The values of H_b are 0.2, 0.4, …, 5.0 km and the values of $\rho_{hv}^{(min)}$ are 0.80, 0.82, …, 0.94. The radar reflectivity peak ΔZ and the depth of the ML (in terms of ρ_{hv}) are assumed to be the following functions of $\rho_{hv}^{(min)}$:

$$\Delta Z \text{ (dB)} = 4.27 + 6.89\left[1 - \rho_{hv}^{(min)}\right] + 341\left[1 - \rho_{hv}^{(min)}\right]^2, \quad (5)$$

$$\Delta H \text{ (km)} = -0.64 + 30.8\left[1 - \rho_{hv}^{(min)}\right] + 315\left[1 - \rho_{hv}^{(min)}\right]^2 + 1115\left[1 - \rho_{hv}^{(min)}\right]^3. \quad (6)$$

The relations (5) and (6) were obtained via statistical analysis of the quasi-vertical profiles (QVP) of Z and CC in the ML at S band in Griffin et al. (2020). Trömel et al. (2019) provided similar relations using QVPs at X band. Other assumptions are formulated as follows:

1) ρ_{hv} is equal to 1 below H_b and above $H_t = H_b + \Delta H$
2) Height of Z maximum is at $H = H_b + 0.8\Delta H$
3) Top of the ML in terms of Z is at $H = H_b + 1.6\Delta H$
4) Vertical gradient β of Z above the ML is equal to 4 dB km^{-1}
5) $Z_{max} = 36$ dBZ
6) $Z_{rain} = Z_{max} - \Delta Z$
7) $Z_{snow} = Z_{rain} - 2.0$ dB
8) Z_{DR} maximum is at the same height as the ρ_{hv} minimum
9) $Z_{DR}^{(max)} = 16.65 - 17.0\,\rho_{hv}^{(min)}$
10) $Z_{DR}^{(rain)} = 0.75 - 0.0623 Z_{rain} + 0.00184 Z_{rain}^2$
11) $Z_{DR}^{(snow)} = 0$ dB for $H > H_t$

These assumptions are consistent with the results reported in the previous studies of the vertical profiles of polarimetric radar variables within the ML by Wolfensberger et al. (2016), Matrosov et al. (2017), Trömel et al. (2019), and Griffin et al. (2020). Most of the researchers tend to agree that the maximum of Z is observed slightly above the CC minimum and the CC dip more objectively represents the melting layer than the Z enhancement. The top of the ML layer in terms of CC corresponds to the freezing level or the height of the wet-bulb temperature 0°C level whereas the bottom of the ML in terms of CC marks the end of snow melting that on average occurs around the temperature of about 3°C (Lundquist et al. 2008) although Heymsfield et al. (2021) reported that the bottom of

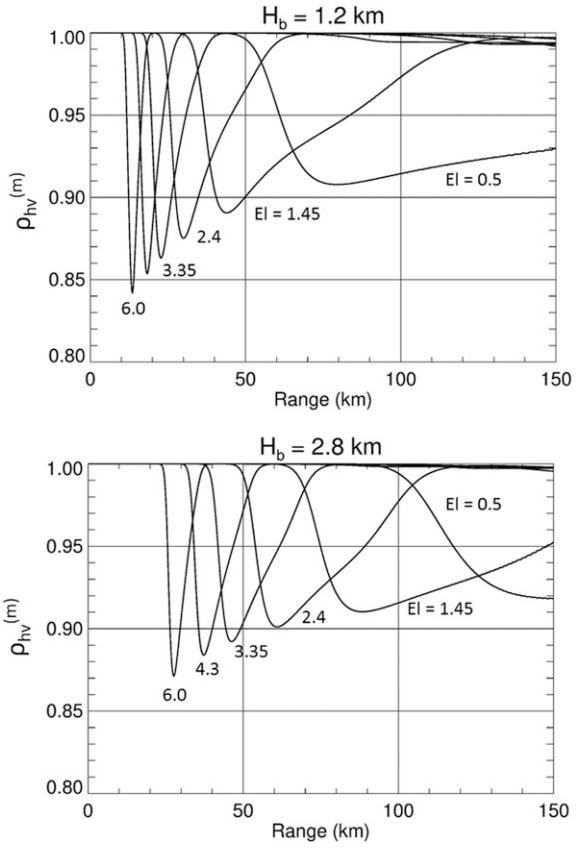

FIG. 5. Simulated radial profiles of $\rho_{hv}^{(m)}$ at different elevations and two heights of the bottom of the (top) ML H_b = 1.2 and (bottom) ML H_b = 2.8 km. Simulations are made for $\rho_{hv}^{(min)} = 0.80$ and radar beamwidth 1.0°.

the ML can be occasionally detected at the temperatures as high as 7°C. The CC minimum generally is observed at the temperature of 1.5° (Matrosov et al. 2017), which is sometimes referred to as the "snow level," which is an altitude where the precipitation type transitions from mostly snow to mostly rain (White et al. 2010). It is well known that the maximal value of Z_{DR} in the ML is strongly correlated with the magnitude of $\rho_{hv}^{(min)}$ (e.g., Griffin et al. 2020; Trömel et al. 2019) and the impact of $Z_{DR}^{(max)}$ on the radial profiles of $\rho_{hv}^{(m)}$ is explicitly taken into account via the $Z_{DR}^{(max)}\left[\rho_{hv}^{(min)}\right]$ dependence specified by assumption (9).

Examples of the radial $\rho_{hv}^{(m)}$ profiles computed for $\rho_{hv}^{(min)} = 0.80$ are shown in Fig. 5 for different elevations and heights of the bottom of the ML (H_b) equal to 1.2 and 2.8 km. These profiles are different for other seven values of $\rho_{hv}^{(min)}$. It is evident from Fig. 5 that range locations and widths of the $\rho_{hv}^{(m)}$ dips vary depending on the antenna elevation and the height of the bottom of the ML [as well as the value of $\rho_{hv}^{(min)}$].

The model profiles will be matched with the observed radial profiles of CC. In fact, there is no need to match the whole observed and model profiles. It is sufficient to match the two of their parameters: the distance where the ML-related CC

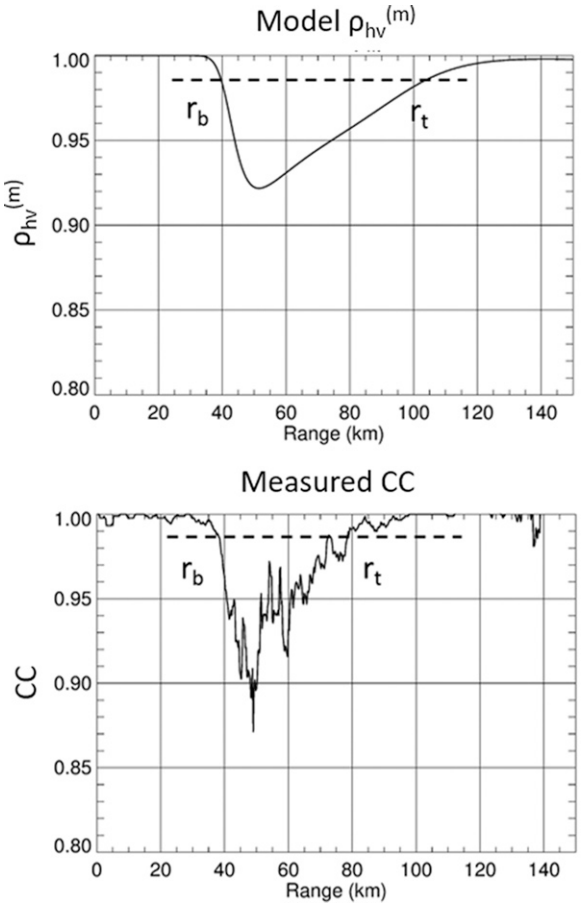

FIG. 6. (top) Simulated and (bottom) measured radial profiles of the cross-correlation coefficient. Threshold value $CC^{(th)} = 0.985$ is depicted with the dashed line. The "strength" of the CC dip is defined as an area between the dashed line and the curve representing radial dependence of CC.

dip starts (r_b) (Fig. 6) and an integral parameter called "strength" S of the CC dip defined as

$$S = \int_{r_b}^{r_t} [CC^{(th)} - CC(r)]dr. \quad (7)$$

The parameter S characterizes the depth of the CC dip and is determined as its area below the CC threshold $CC^{(th)}$ (Fig. 6). In the current version of the algorithm, $CC^{(th)} = 0.985$. This value of $CC^{(th)}$ was determined empirically for the WSR-88Ds and may need adjustment for the polarimetric radars of different types operating at C or X bands. As Fig. 6 shows, the distance r_b and integral parameter S can be reliably estimated even for quite "noisy" measured radial profiles of CC. For any given antenna elevation, the model parameters r_b and S are computed for 25 values of the height of the ML bottom H_b and 8 values of $\rho_{hv}^{(min)}$ and stored in the two lookup tables for r_b and S with dimensions 25×8. Each element in the table is assigned indexes ir (for r_b) and is (for S).

For any given elevation, the matching routine compares the estimated parameters r_b and S of the measured radial profile

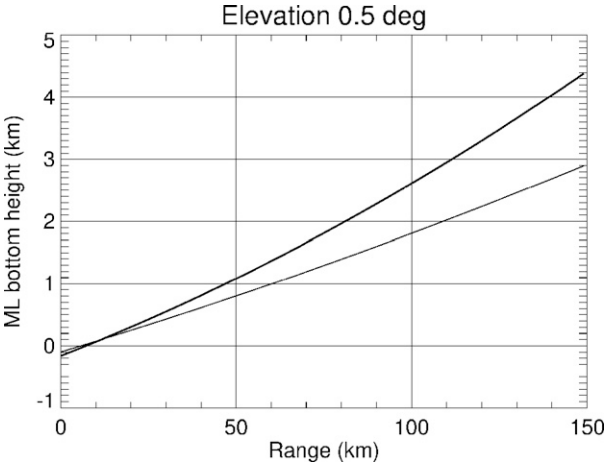

FIG. 7. The dependence of the ML bottom height on the starting distance of the CC dip for antenna elevation 0.5° and deep and shallow ML (thick and thin curves, respectively).

of CC with the ones in the two lookup tables and identifies the closest model pair of indexes ir and is. Then, the height of the bottom of the ML H_b is computed as

$$H_b = a(is) + b(is)r_b(ir, is) + c(is)r_b^2(ir, is), \quad (8)$$

where **a**, **b**, and **c** are predetermined eight-element vectors for a given elevation, which are also stored along with the two lookup tables. Note that the value of H_b can vary quite significantly for a given r_b depending on the thickness or depth of the ML. This is a result of the radar beam broadening so that the dependence of H_b on r_b cannot be quantified via simple geometric considerations. Figure 7 shows that the dependence of H_b on r_b is a function of the ML strength index.

For a given r_b, H_b is higher for thicker (or stronger) ML. The difference between H_b for the strongest and weakest ML can exceed 1.5 km at the range of 150 km from the radar for elevation 0.5°. This means that the correct estimation of the ML strength (or index is) is very important. The thickness of the ML ΔH is determined by index is [or $\rho_{hv}^{(min)}$] according to Eq. (6) and the height of the top of the ML H_t is determined as $H_t = H_b + \Delta H$.

Lookup tables for r_b and S as well as vectors **a**, **b**, and **c** can be generated very quickly for an arbitrary antenna elevation angle, and the model assumptions 1–11 can be changed if needed in order to optimize the algorithm performance. It is important that our model based on Eqs. (2)–(4) does not require horizontal uniformity of the ML along a full radar radial. However, it requires radial uniformity within the CC dip for a given elevation angle (Fig. 5). This allows capturing radial variability of the ML parameters H_b and ΔH due to the use of the data collected at different elevations with the CC dips occurring at different distances from the radar—a feature missing in all previous ML detection algorithms. Radial profiles of CC at various azimuths are treated independently, which ensures that azimuthal variability of the ML is taken into account as well.

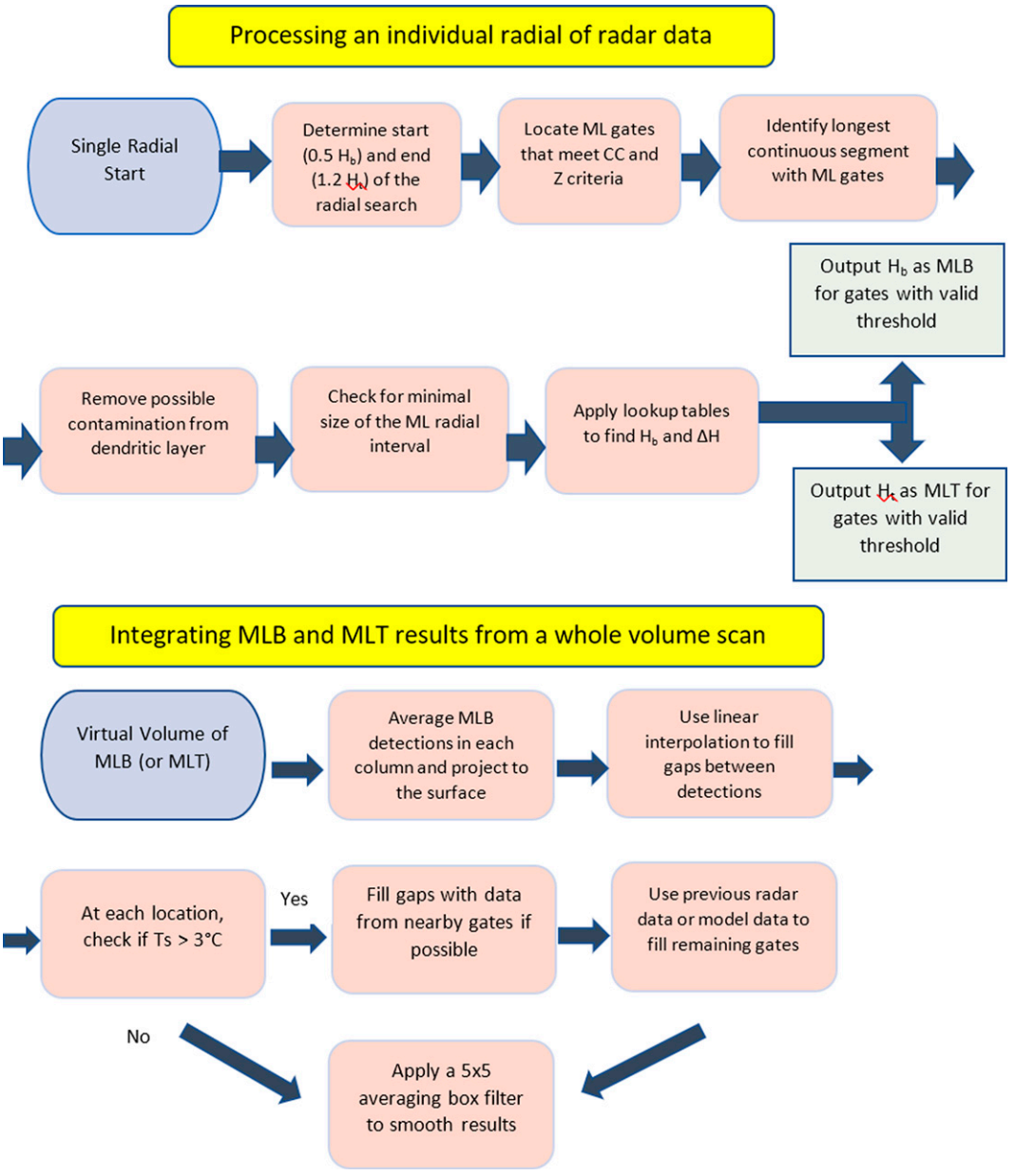

FIG. 8. A flowchart of the new MLDA algorithm.

A flowchart of the new melting-layer detection algorithm is presented in Fig. 8. Locating the data in the radial that we match to the model profile is accomplished by identifying the locations in the radial that have a CC between 0.985 and 0.80 while also having a reflectivity between 20 and 50 dBZ. While this criterion does an adequate job of identifying ML locations in light rain, freezing rain or drizzle often have reflectivity values below 20 dBZ. Hence, in addition, we also identify range gates with Z between 10 and 20 dBZ and a stronger CC depression between 0.97 and 0.80. A major contaminant of the CC data is ground clutter. We use two separate methods to reduce contamination by ground clutter. We first limit the search for ML locations to areas near the most recent ML detection (or model data) by removing any locations identified by the above criteria that correspond to the heights lower than $0.5H_b$ and higher than $1.2H_t$ where H_b and H_t are estimated either from the previous scan or from the model. For example, if previously estimated H_b = 1.0 km and H_t = 1.5 km, then we would search for the ML range gates in the radial interval corresponding to the ML heights between 0.5 and 1.8 km. We also limit the search by identifying the longest continuous segment of ML detections in the radial. The process assumes that the ML in the data is the longest continuous detected segment of lowered CC and elevated Z. Because we noticed that some of the ML range segments may contain gates where the data briefly fail to meet our criteria, we allow for a significant number of missing gates (20 gates or about

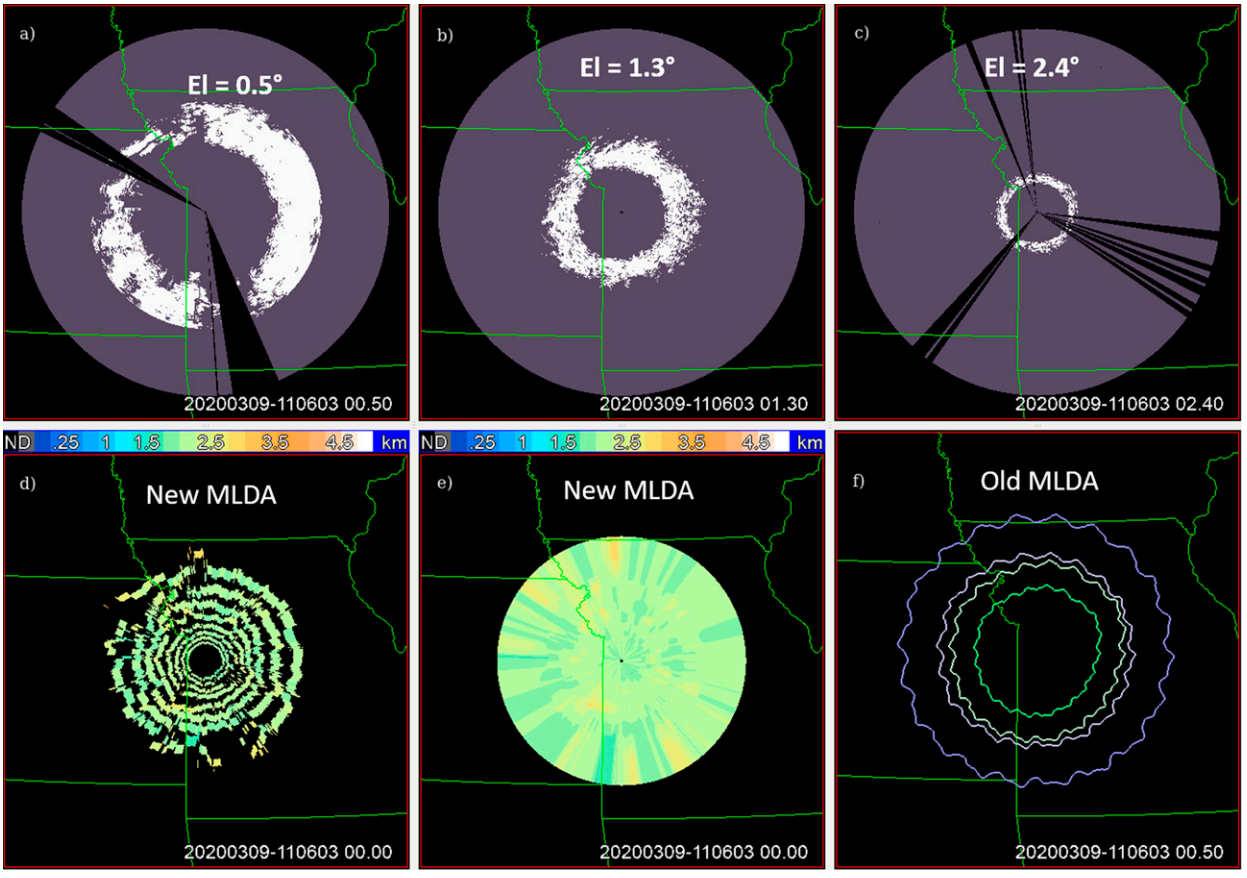

FIG. 9. Reconstruction of the map of the ML bottom height for the event on 9 Mar 2020. (a)–(c) Locations of the ML pixels on PPIs at El = 0.5°, 1.3°, and 2.4°, respectively. The map of the ML bottom height H_b reconstructed from eight antenna elevations (d) before and (e) after interpolation. (f) The contours of R_{bb}, R_b, R_t, and R_{tt} (see Fig. 1b).

5 km) or data holes when computing the longest continuous detected segment. These two methods allow the algorithm to remove most ground clutter contamination from the data.

Another possible source of contamination is a frequently observed reduction of CC in the DGL, which is located well above the ML and is generally centered at −15°C. The DGL produces a smaller drop in the CC and lower Z than the ML does. The $1.2H_t$ criterion mentioned above is usually sufficient to eliminate DGL contamination. To remove any possible residual DGL contamination, we reevaluate the data saved as the longest continuous radial segment with depressed CC. The data are separated into intervals with data holes no larger than five gates (~1.25 km) and each of these intervals is evaluated to determine the location of the minimum CC in the segment. If the location of the minimum CC is over a point with a surface temperature below 0°C, there is a chance that this detection was created by the DGL rather than the ML. To filter out these false ML designations, we subject the data at the minimum CC location to a more stringent test by checking that CC does not drop below the empirically determined threshold 0.93 + 0.03 SNR (dB), where SNR is the signal-to-noise ratio.

Once the above checks and limits are applied, the first gate with a positive ML detection is considered to signify the bottom of the melting layer (r_b) and the last gate detected is considered to be related to the top of the melting layer (r_t). The strength (S) of the melting layer is computed by summing the CC difference from the value $CC^{(th)}$ as in Eq. (7) and the combination of r_b and S determines the depth of the melting-layer ΔH using the appropriate lookup table. The indexes of r_b and S are used in Eq. (8) to determine the true value of the ML bottom height (H_b), and the value of H_t is determined as $H_t = H_b + \Delta H$.

The process used for converting each individual radial into the final 2D plot of the ML height is the same for both the ML bottom (H_b) and ML top (H_t). For a given elevation and azimuth, the range gates identified as corresponding to the ML between H_b and H_t are projected onto the horizontal plane and painted with a color corresponding to either H_b or H_t color code (for the H_b or H_t 2D maps, respectively). Note that all projected pixels within a given ML radial segment have the same color for a given antenna elevation and azimuth. Combining the ML pixels from all azimuths for a single tilt results in a "ring" around the radar collocated with the ML CC dip at this tilt and multiple concentric rings corresponding to different tilts are assembled together as shown in Fig. 9d.

The rings corresponding to higher elevations (say, those between 2.4° and 5.0°) may overlap, but the rings from the

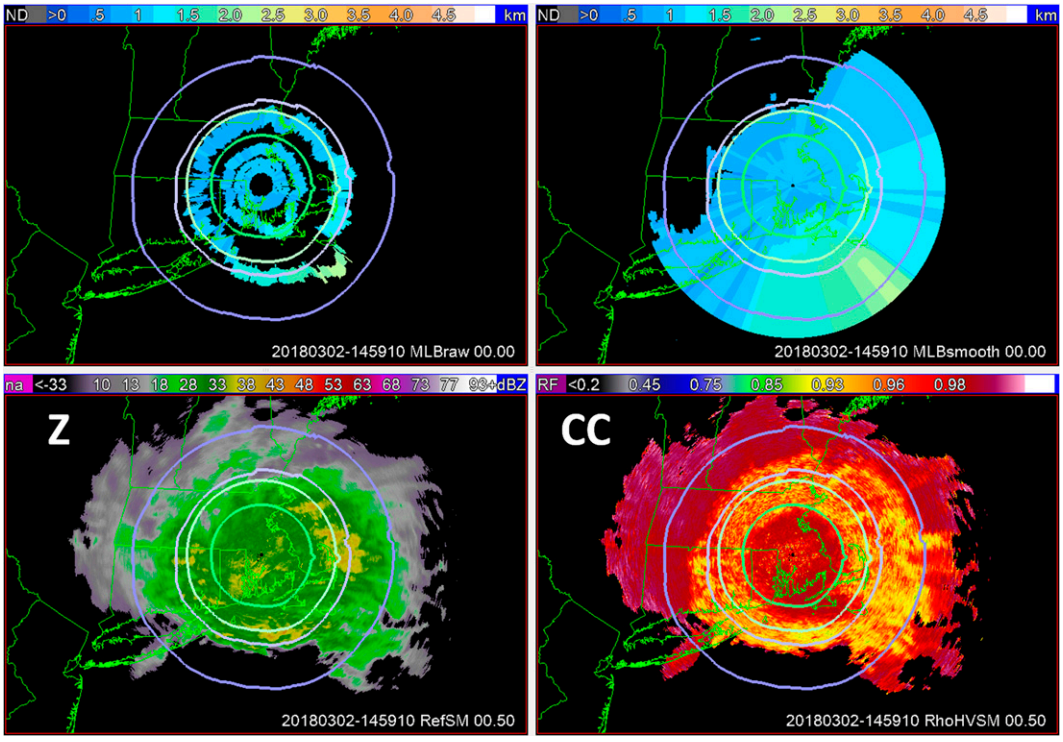

FIG. 10. The maps of (top) the heights of the ML bottom H_b before and after interpolation/extrapolation and (bottom) Z and CC at El = 0.5° for the storm observed by the KOKX WSR-88D on 2 Mar 2018. The contours of R_{bb}, R_b, R_t, and R_{tt} are overlaid on all panels.

lower elevations are commonly separated by gaps, which have to be filled to make a continuous ML 2D map. The gaps between elevations are filled using a simple linear interpolation while the data corresponding to the overlapped rings are combined via simple averaging (Fig. 9e).

The absence of the ML signature aloft means that either the whole vertical column of the atmosphere is at subfreezing temperatures or precipitation is very shallow or the ML is below the lowest elevation beam, which is common at longer distances from the radar. In this situation, we use a surface temperature T_s from the model to make a guess about the height of the ML. For example, if $T_s > 3$°C then it is very likely that the ML exists at some height although the radar may not detect it. For instance, if T_s at the radar location exceeds 3°C we can confidently interpolate the ML data into the radar cone of silence from the surrounding areas where the radar data exist. Similarly, we extrapolate the farthest reliably estimated ML height outward along the radial provided that $T_s > 3$°C out to 150–200 km in range. If no melting-layer data exist for an entire radial, we use a 2-h time averaged value of the ML height. Finally, we apply a 5×5 averaging box filter to spatially smooth the melting-layer-height results.

3. Examples of the new MLDA products

The initial version of a new MLDA was implemented in C++ and tested for a number of cold-season events. Herein, we show three examples of the ML height maps generated by the operational prototype of MLDA. The first example illustrates the ML map construction for the case on 9 March 2020 with spatially uniform ML observed with the KEAX WSR-88D (Fig. 9). Figures 9a–c illustrate locations of the CC dips (or radar gates associated with the melting layer) on PPIs at three elevations: 0.5°, 1.3°, and 2.4°. For every ML segment at each elevation and azimuth, the heights of the bottom and top of the ML (H_b and H_t) are determined using the new MLDA algorithm. These designations are represented as the color-coded maps of H_b and H_t. The map of H_b assembled from the data collected at the 8 lowest antenna elevations (0.5°, 0.9°, 1.3°, 1.8°, 2.4°, 3.1°, 4.0°, and 5.1°) is displayed in the Fig. 9d. It shows that H_b varies very slightly between 2.0 and 2.5 km over a large radar coverage area for this event. The interpolation/extrapolation routine fills the gaps between the color-coded pixels and extrapolates the results up to the 200-km range from the radar so that the final new MLDA product is generated (Fig. 9e). For comparison, the output of the existing MLDA algorithm implemented on the WSR-88D network is displayed in Fig. 9f, which is similar to the one in Fig. 2.

The next example contains a sloping melting layer observed during the storm observed with the Boston (KBOX) WSR-88D around 1505 UTC 2 March 2018 (Fig. 10). The "rings" of CC dips show pronounced asymmetry as opposed to the previous case. The regions of depressed CC at lower elevations are observed at significantly longer distances from the radar in the southern and eastern ocean sectors with the corresponding H_b heights exceeding 2 km whereas H_b in the

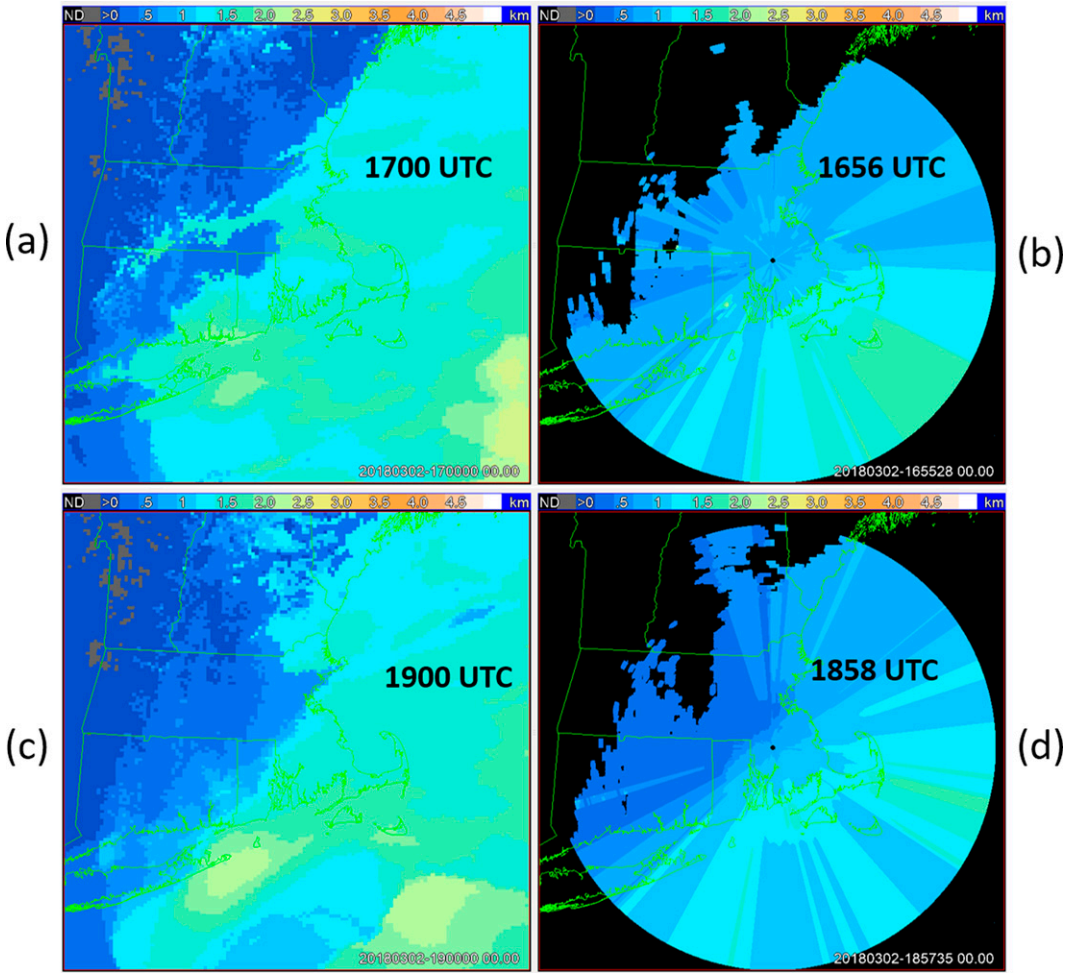

FIG. 11. 2D maps of (left) the height of the 0°C wet-bulb temperature isotherm from the HRRR model and (right) the height of the bottom of the ML retrieved from the KOKX WSR-88D at around 1700 and 1900 UTC 2 Mar 2018.

northern and western land sectors is generally below 1 km. This is consistent with weather observations and the spatial distribution of temperature retrieved from the High-Resolution Rapid Refresh (HRRR) model indicating that the ocean sector is warmer than the land one. The 2D maps of the height H_{fl} of the freezing level corresponding to the 0°C wet-bulb temperature isotherm from the HRRR model and of the height of the bottom of the ML H_b retrieved from the KBOX WSR-88D at around 1700 and 1900 UTC 2 March 2018 are displayed in Fig. 11. The spatial features of the model H_{fl} map and the radar H_b map are very similar although H_{fl} is about half a kilometer higher than H_b, as expected. Both maps indicate general decrease of the ML height from southeast to northwest and progression of the cold front to the east during a 2-h time interval. Radial streaks in the radar ML H_b map are caused by interpolation between the low CC rings at lower elevations and by extrapolation of the results to the distance of 200 km from the radar. There is no doubt that the quality of the ML height determination degrades beyond the ranges 100–150 km but we believe that the extrapolation of the ML detection results up to 200 km may have some practical value, particularly for optimization of the QPE algorithms, which use different radar rainfall relations in pure rain and areas affected by "brightband" contamination (Ryzhkov and Zrnić 2019).

Note that the overlaid contours of R_{bb}, R_b, R_t, and R_{tt} in Fig. 10 obtained from the existing WSR-88D MLDA are almost symmetric and do not reflect significant change of the ML height along the north–south or west–east directions. This is not surprising because the data input to the existing MLDA algorithm is formed at very close distances to the KBOX radar (less than 30 km) where the ML is relatively uniform.

Finally, we demonstrate our new algorithm performance for the case with a sharp frontal boundary separating snow and rain at the surface. The methodology described so far assumes a relatively gradual change of the height of the ML. This is usually not the case in the proximity of the frontal boundaries where it changes abruptly, say, from 2 km down to 0 km.

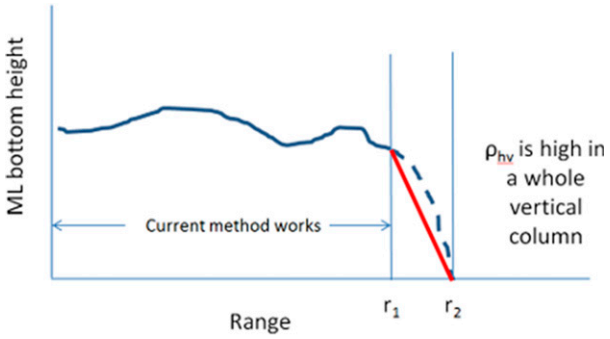

FIG. 12. Conceptual plot explaining the methodology for estimating the ML height in the proximity of the frontal boundary.

In such a situation, we can capitalize on the fact that on the "cold" side of the frontal boundary the value of the cross-correlation coefficient CC is close to 1 in a full depth of the cloud and such boundary is very well delineated in terms of CC. To address such a situation, we identify areas with pure dry snow in a full vertical column of the cloud by checking that CC is very close to 1 at all antenna elevations and assume that the ML does not exist in that area (i.e., $H_b = H_t = 0$ km). Let us say that such an area of dry snow is found beyond the distance r_2 from the radar at a given azimuthal direction (Fig. 12). Then we have to ignore the H_b results retrieved from the MLDA procedure described so far at the distances $> r_1 = r_2 - \Delta$ and linearly interpolate $H_b(r_1)$ down to the ground at r_2 as shown by the red line in Fig. 12.

An example of the new MLDA products for a winter event with sharp rain–snow frontal boundary observed by the Milwaukee KMKX WSR-88D on 11 January is illustrated in Figs. 12 and 13. The PPI of Z does not provide any clue on the location of the rain–snow line whereas CC at El = 0.5° clearly delineates this transition northwest from the radar (bottom panels in Fig. 13). The maps of the ML H_b before and after interpolation in the top panels of Fig. 13 display ML rapidly descending to the surface through the frontal boundary. The absence of the ML (pure snow in a vertical column) is shown in black in the H_b map. Similar maps taken about one hour later show good temporal continuity of the ML designation results with the frontal boundary shifting eastward (Fig. 14).

As was mentioned in Introduction, the majority of the previous techniques for determination of the height of the ML use the data collected in the genuine RHI mode of operation when the radar beam is scanning in the vertical plane. The reconstructed vertical RHI cross sections generated from the series of PPIs do not provide sufficient vertical resolution required to determine the height of the ML even at very close ranges. An example of a composite reconstructed RHI is presented in Fig. 15 for the storm observed by the KBMX WSR-88D on 12 February 2014. It is obvious that it is not possible to determine the heights of the bottom and top of the ML from the reconstructed RHI with a good accuracy, particularly

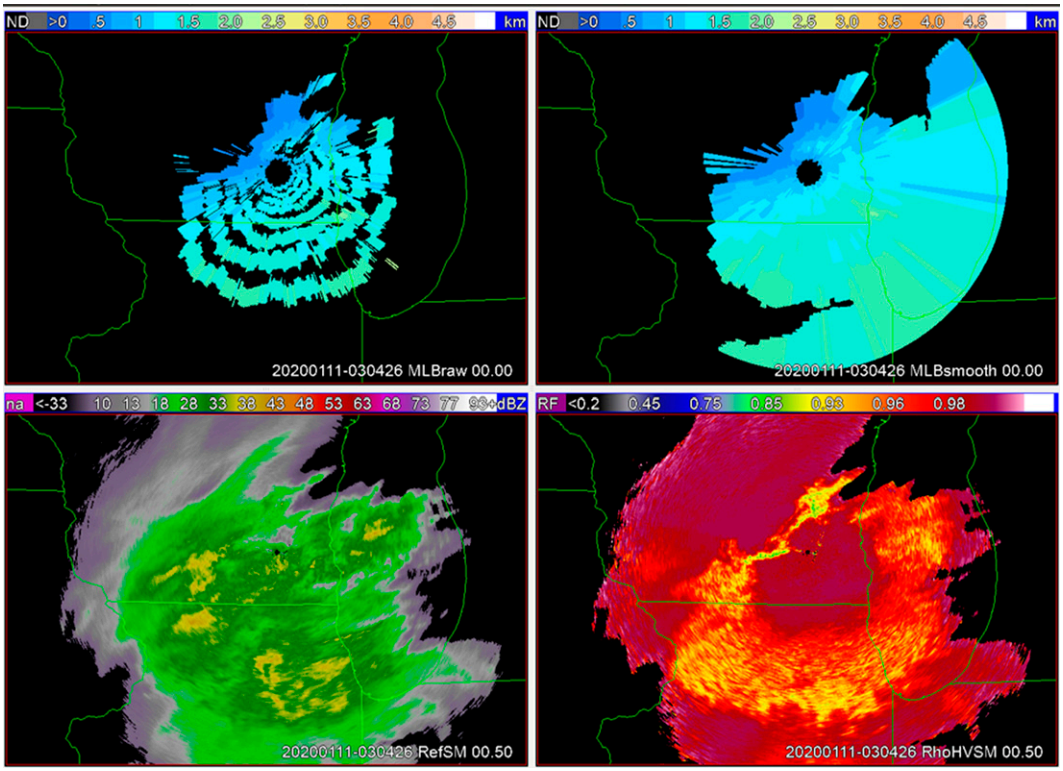

FIG. 13. (bottom) The fields of Z and CC and (top) height of the ML bottom before and after interpolation/extrapolation for the event on 11 Jan 2020 observed with the KMKX WSR-88D at 0304 UTC.

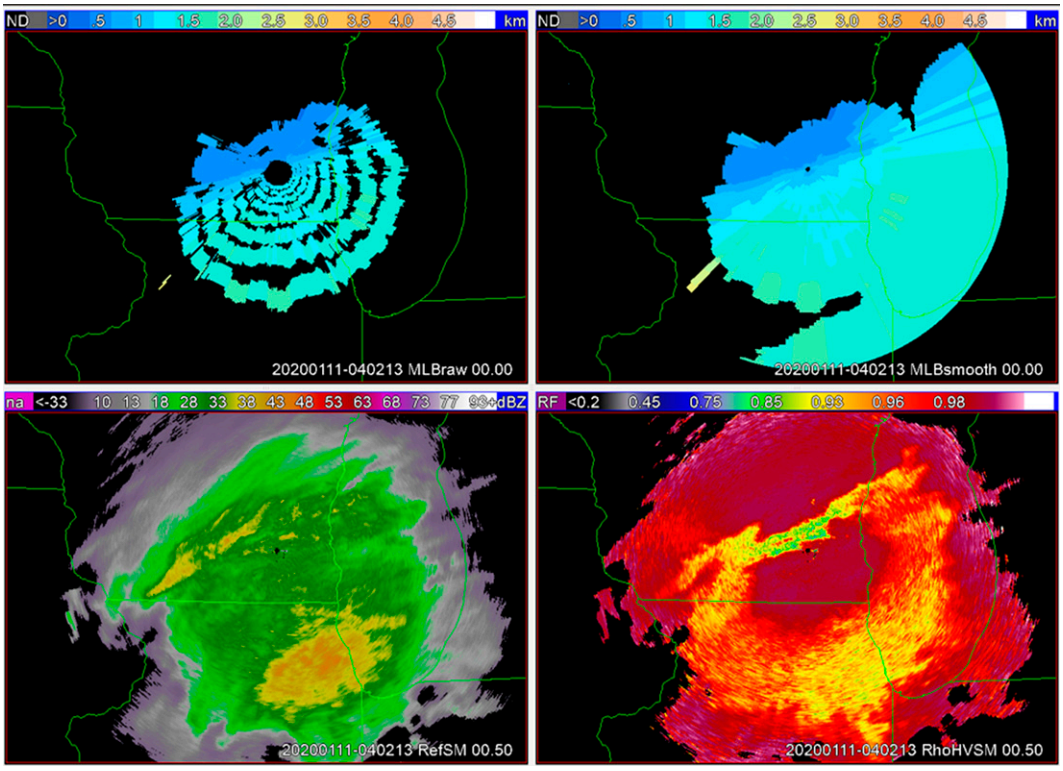

FIG. 14. As in Fig. 13, but ~1 h later (at 0402 UTC).

at longer distances from the radar. The radial dependencies of H_b and H_t retrieved from the new MLDA are overlaid on the CC panel of reconstructed RHI. They clearly exhibit the range variability of the ML top and bottom up to distances beyond 100 km with an accuracy much better than the vertical size of the radar sampling volume, which is more than 1.7 km at such ranges for the width of the radar beam 1.0°. This is not surprising because the distance r_b to the beginning of the CC dip can be measured with high accuracy which ensures high-quality determination of H_b according to Fig. 7 provided that the strength S of the ML is reliably estimated. Indeed, if the distance r_b is measured to an accuracy of 5 km, then the corresponding uncertainty in the H_b estimation for r_b = 100 km using the curves in Fig. 7 [or Eq. (8)] is only 0.1–0.2 km depending on the value of S.

4. Validation of the new MLDA

Estimation of the accuracy of the ML height determination is an important part of the algorithm evaluation. There are various possible ways to quantify such an accuracy. One of them is to use the HRRR model data. The problem is that the NWP models are less reliable in the areas of large spatial gradients of the ML height, particularly near frontal boundaries. Another option is to use ground-based vertically looking radars or airborne/spaceborne nadir-looking radars, which usually detect the "bright band" and measure its height with sufficient accuracy (e.g., Matrosov et al. 2017). A comprehensive validation effort is beyond the scope of this study and this article, which is focused on the description of the new MLDA algorithm. This will be performed in the near future.

As an initial validation effort, we checked the consistency of the new MLDA product with the output of the QVP technique that provides a very robust representation of the ML at relatively close distances to the radar. The QVP methodology was introduced by Ryzhkov et al. (2016) and further refined by Tobin and Kumjian (2017). According to the initial version of the QVP methodology, vertical profiles of radar variables are generated by azimuthal averaging of the radar data in a full circle at a single high elevation (usually between 10° and 20°). The data are presented in a height versus time format, which represents temporal evolution of the vertical structure of the storm with high vertical resolution. Tobin and Kumjian (2017) modified the original QVP technique by suggesting the "range-defined" QVP (RD-QVP), which combines QVPs at multiple elevations. The RD-QVP technique uses radar data from the distances within 50 km from the radar. Therefore, every vertical profile is a result of averaging over the echo in a circular area with a 50-km radius centered on the radar.

The QVPs of polarimetric radar variables through the melting layer have been thoroughly investigated in the studies of Trömel et al. (2019), Allabakash et al. (2019), and Griffin et al. (2020), which demonstrated that the heights of the ML top and bottom (in terms of CC) can be estimated with an accuracy of about 0.1 km within the QVP area. Therefore, RD-QVP can serve as a good reference to evaluate the quality of

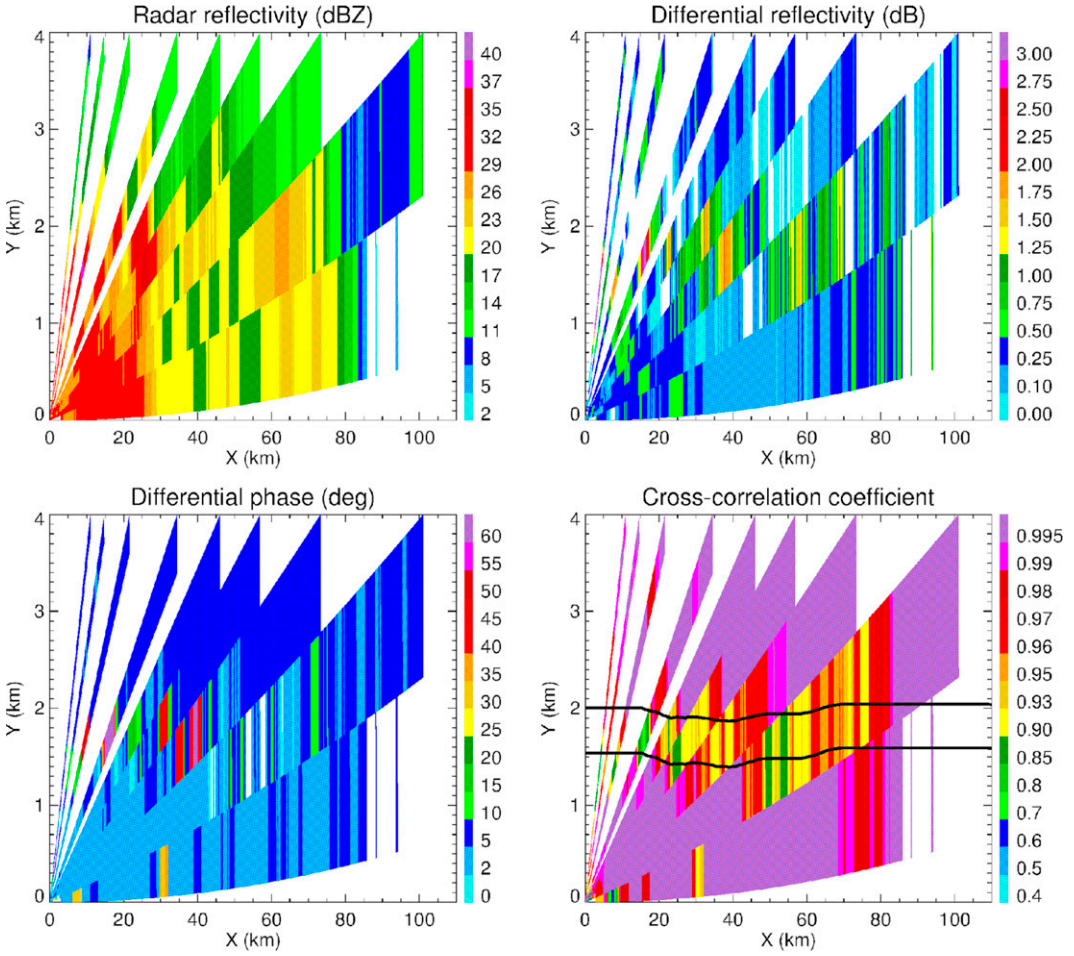

FIG. 15. Reconstructed RHIs of (top left) Z, (top right) Z_{DR}, (bottom left) Φ_{DP}, and (bottom right) CC with overlaid lines indicating the heights of the top and bottom of the ML at Az = 150° for the KBMX case on 12 Feb 2014.

the new MLDA. To make the QVP–MLDA comparison, the heights of the top and bottom of the ML retrieved by MLDA have been averaged over the same area for which the QVP product is generated.

The examples of such a comparison are shown in Fig. 16 for four stratiform rain events observed by different WSR-88Ds. In all panels, the RD-QVPs of CC are displayed in a height versus time format and the new MLDA estimates of H_b and H_t are depicted as overlaid green and blue lines, respectively. It is evident that the MLDA and RD-QVP products are well aligned with the temporal dependences of H_b and H_t following the bottom and top of the CC minimum revealed by RD-QVP.

A more detailed quantitative comparison of the MLDA and RD-QVP outputs for these four cases shows that MLDA slightly underestimates the heights of the ML top and bottom. The average negative biases in the estimation of the heights of the ML top and bottom for four events are 128 and 107 m, respectively.

Note that the RD-QVP–MLDA comparison can be used as a test of the new MLDA performance only at distances less than 50 km from the radar. Different validation methodologies should be utilized at longer distances, which will be a topic of further research.

5. Discussion and conclusions

The suggested new MLDA algorithm uses the CC information almost exclusively for detection of the melting layer in contrast with the existing WSR-88D method that also directly utilizes Z and Z_{DR} data (Giangrande et al. 2008). Although CC is the best radar variable for the ML detection, Z_{DR} also exhibits strong signatures in the ML and we plan to use it in a more refined and extended future version of the algorithm. The CC depression associated with the ML should not be mixed up with the CC decrease attributed to ground clutter contamination at close distances from the radar and the dendritic growth layer at longer ranges. The procedures to filter out these false ML designations are embedded in the algorithm as described in section 2 but their further improvement is expected.

The underlying model of the ML illustrated in Fig. 4 is valid for stratiform clouds but not for convective cores. Running

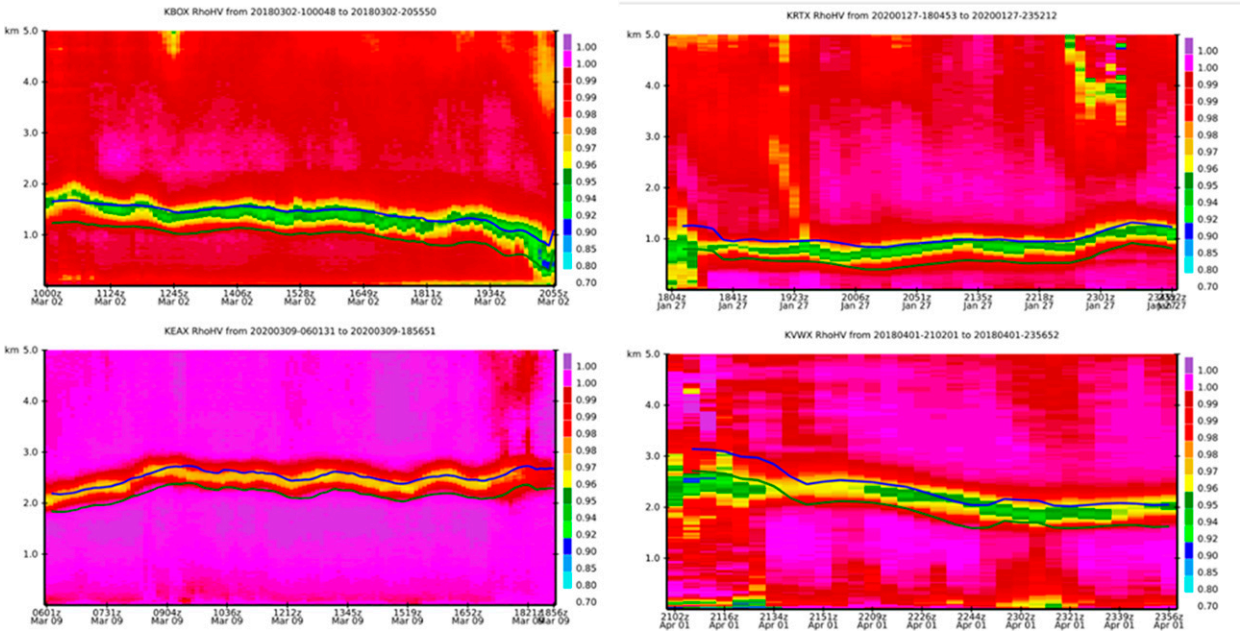

FIG. 16. RD-QVPs of CC for four events with the new MLDA estimates of H_b and H_t depicted as overlaid green and blue lines, respectively.

the new MLDA for a multitude of cold-season events shows that relatively weak embedded convection does not significantly affect the performance of the algorithm mainly due to the use of aggressive spatial median filtering that eliminates occasional "blips" associated with weak and localized convection typical for cold-season events. The cases with deep warm-season convection have to be treated differently if the algorithm is applied for all seasons. Most likely, the areas of deep convection (such as squall lines of the mesoscale convective systems) should be identified first and the new MLDA algorithm will be applied only outside of the convective areas.

Another important problem to be addressed is determination of the ML height in the radar echo gaps or larger echo-free areas. If the echo gap is relatively small then it can be filled with the radar ML designations from the neighboring echo regions. However, if the echo-free area is large then resorting to the model information is inevitable. Some simplistic procedures such as utilization of the surface temperature from the model are already implemented in the algorithm as discussed in section 2. However, a more sophisticated scheme for merging the radar and model data has to be developed.

Summarizing, we can conclude that a principally novel algorithm for melting-layer detection and determination of its height has been developed. It is based on using the cross-correlation coefficient (CC) information collected at the lowest elevation radar scans and explicitly takes into account the impact of beam broadening on the spatial distribution of CC at longer distances from the radar. As a result, the 2D maps of the height of the ML top and bottom are generated at ranges up to 150–200 km from the radar. It is important that the new MLDA captures both azimuthal and radial variability of the ML height with respect to the radar location.

The initial version of the new algorithm was implemented in C++ and tested for a large number of cold-season events with low ML and with different degrees of spatial nonuniformity including cases with sharp frontal boundaries and rain–snow transitions. The new MLDA demonstrated robust performance and the resulting 2D maps of the ML heights exhibit a good degree of spatial and temporal continuity. The MLDA output shows consistency with the RD-QVP products and model designation of the melting layer. A more comprehensive validation of the new MLDA products and their merging with the HRRR model results will be addressed in the future studies.

Acknowledgments. Funding was provided by NOAA/Office of Oceanic and Atmospheric Research under NOAA–University of Oklahoma Cooperative Agreement NA16OQR4320115, U.S. Department of Commerce, as well as the Radar Product Improvement program run by the National Weather Service Radar Operations Center.

Data availability statement. All data used for this study are available upon request.

REFERENCES

Allabakash, S., S. Lim, and B.-J. Jang, 2019: Melting layer detection and characterization based on range height indicator–quasi vertical profiles. *Remote Sens.*, **11**, 2848, https://doi.org/10.3390/rs11232848.

Boodoo, S., D. Hudak, N. Donaldson, and M. Leduc, 2010: Application of dual-polarization radar melting-layer detection algorithm. *J. Appl. Meteor. Climatol.*, **49**, 1779–1793, https://doi.org/10.1175/2010JAMC2421.1.

Brandes, E., and K. Ikeda, 2004: Freezing-level estimation with polarimetric radar. *J. Appl. Meteor.*, **43**, 1541–1553, https://doi.org/10.1175/JAM2155.1.

Giangrande, S. E., J. M. Krause, and A. V. Ryzhkov, 2008: Automatic designation of the melting layer with a polarimetric prototype of the WSR-88D radar. *J. Appl. Meteor. Climatol.*, **47**, 1354–1364, https://doi.org/10.1175/2007JAMC1634.1.

Griffin, E., T. Schuur, and A. Ryzhkov, 2020: A polarimetric radar analysis of ice microphysical properties in melting layers of winter storms using S-band quasi-vertical profiles. *J. Appl. Meteor. Climatol.*, **59**, 751–767, https://doi.org/10.1175/JAMC-D-19-0128.1.

Heymsfield, A., A. Bansemer, A. Theis, and C. Schmitt, 2021: Survivals of snow in the melting layer: Relative humidity influence. *J. Atmos. Sci.*, **78**, 1823–1845, https://doi.org/10.1175/JAS-D-20-0353.1.

Lundquist, J. D., P. Neiman, B. Martner, A. White, D. Gottas, and F. Ralph, 2008: Rain versus snow in Sierra Nevada, California: Comparing Doppler profiling radar and surface observations of melting level. *J. Hydrometeor.*, **9**, 194–211, https://doi.org/10.1175/2007JHM853.1.

Matrosov, S., K. Clark, and D. Kingsmill, 2007: A polarimetric radar approach to identify rain, melting layer, and snow regions for applying corrections to vertical profiles of reflectivity. *J. Appl. Meteor. Climatol.*, **46**, 154–166, https://doi.org/10.1175/JAM2508.1.

——, R. Cifelli, A. White, and T. Coleman, 2017: Snow-level estimates using operational polarimetric weather radar measurements. *J. Hydrometeor.*, **18**, 1009–1019, https://doi.org/10.1175/JHM-D-16-0238.1.

Park, H.-S., A. Ryzhkov, D. Zrnić, and K.-E. Kim, 2009: The hydrometeor classification algorithm for the polarimetric WSR-88D. Description and application to an MCS. *Wea. Forecasting*, **24**, 730–748, https://doi.org/10.1175/2008WAF2222205.1.

Reeves, H., A. Ryzhkov, and J. Krause, 2016: Discrimination between winter precipitation types based on spectral-bin microphysical modeling. *J. Appl. Meteor. Climatol.*, **55**, 1747–1761, https://doi.org/10.1175/JAMC-D-16-0044.1.

Ryzhkov, A., 2007: The impact of beam broadening on the quality of radar polarimetric data. *J. Atmos. Oceanic Technol.*, **24**, 729–744, https://doi.org/10.1175/JTECH2003.1.

——, and D. Zrnić, 2019: *Radar Polarimetry for Weather Observations.* Springer, 486 pp.

——, P. Zhang, H. Reeves, M. Kumjian, T. Tschallener, C. Simmer, and S. Trömel, 2016: Quasi-vertical profiles—A new way to look at polarimetric radar data. *J. Atmos. Oceanic Technol.*, **33**, 551–562, https://doi.org/10.1175/JTECH-D-15-0020.1.

——, and Coauthors, 2017: Estimation of depolarization ratio using radars with simultaneous transmission/reception. *J. Appl. Meteor. Climatol.*, **56**, 1797–1816, https://doi.org/10.1175/JAMC-D-16-0098.1.

Schuur, T., H.-S. Park, A. Ryzhkov, and H. Reeves, 2012: Classification of precipitation types during transitional winter weather using the RUC model and polarimetric radar retrievals. *J. Appl. Meteor. Climatol.*, **51**, 763–779, https://doi.org/10.1175/JAMC-D-11-091.1.

Shusse, Y., T. Maesaka, K. Ikeda, and K. Iwanami, 2019: Polarimetric radar observation of the melting layer in a winter precipitation system associated with a south-coast cyclone in Japan. *J. Meteor. Soc. Japan*, **97**, 375–385, https://doi.org/10.2151/jmsj.2019-021.

Song, J., S. Yum, S. Park, K. Kim, K. Park, and S. Joo, 2021: Climatology of melting layer heights estimated from cloud radar observations at various locations. *J. Geophys. Res. Atmos.*, **126**, e2021JD034816, https://doi.org/10.1029/2021JD034816.

Tabary, P., A. Le Henaff, G. Vulpiani, J. Parent-du-Chatelet, and J. J. Gourley, 2006: Melting layer characterization and identification with a C-band dual-polarization radar: A long-term analysis. Preprints, *Fourth European Conf. on Radar in Meteorology and Hydrology*, Barcelona, Spain, Servei Meteorològic de Catalunya, 17–20.

Tobin, D., and M. Kumjian, 2017: Polarimetric radar and surface-based precipitation-type observations of ice pellet to freezing rain transitions. *Wea. Forecasting*, **32**, 2065–2082, https://doi.org/10.1175/WAF-D-17-0054.1.

Trömel, S., A. Ryzhkov, B. Hickman, K. Muhlbauer, and C. Simmer, 2019: Polarimetric radar variables in the layers of melting and dendritic growth at X band—Implications for a nowcasting strategy in stratiform rain. *J. Appl. Meteor. Climatol.*, **58**, 2497–2522, https://doi.org/10.1175/JAMC-D-19-0056.1.

White, A., D. Gottas, A. Henkel, P. Neinman, F. Ralph, and S. Gutman, 2010: Developing a performance measure for snow-level forecasts. *J. Hydrometeor.*, **11**, 739–753, https://doi.org/10.1175/2009JHM1181.1.

Wolfensberger, D., D. Scipion, and A. Berne, 2016: Detection and characterization of the melting layer based on polarimetric radar scans. *Quart. J. Roy. Meteor. Soc.*, **142**, 108–124, https://doi.org/10.1002/qj.2672.